

The Island of Inversion at $N=40$

Martha Liliana Cortés

RIKEN Nishina Center, Wako, Saitama 351-0198, Japan

.....
 Our understanding of the structure of atomic nuclei largely derives from the nuclear shell model, which has proven widely successful. Further test to our interpretation of the nuclear properties is provided by the study of shell evolution. Increasing experimental information has shown that the nuclear energy shells change when going towards the most exotic nuclei, in turn making some shell closures disappear while others arise. In particular, the $N = 40$ sub-shell closure has been the subject of extensive research due to the emergence of a so-called Island of Inversion, where deformed intruder configurations dominate the wave function of the ground state. An overview of recent experimental results in the $N = 40$ Island of Inversion, particularly those performed with the combination of the MINOS hydrogen target and the DALI2 γ -ray array at the RIBF are discussed.

Subject Index xxx, xxx

arXiv:2412.16940v1 [nucl-ex] 22 Dec 2024

1 Introduction

The concept of nuclear shell structure plays a key role in our description of the atomic nucleus. In this model, nucleons occupy discrete energy levels determined by the effective central potential. Sizable gaps between groups of energy levels disfavour the excitation of particles to higher lying orbitals, giving rise to the so-called magic numbers. A complete understanding of the magic numbers experimentally observed in stable isotopes (2, 8, 20, 28, 50, 82, 126) requires to consider not only a harmonic oscillator-type central potential, but also to include the spin-orbit interaction [1, 2].

In the last decade an increasing amount of experimental information has been gathered which indicates that the nuclear shell closures are modified when going away from the valley of stability [3–5]. A particular interesting example is the disappearance of the $N = 20$ magic number and the formation of a so-called Island of Inversion (IoI) around ^{32}Mg , where deformed intruder configurations become the ground state. Different theoretical interpretations have been developed, and it has been identified that Islands of Inversion are formed due to quadrupole correlations which maximize energy gains with multiparticle-multihole excitations across the gap at the magic numbers [5].

Another region of the nuclear chart that has attracted much interest due to the development of an IoI is the one of the neutron-rich isotopes around $N = 40$, which corresponds to a shell closure of the harmonic oscillator potential. Investigations on the possible magicity of ^{68}Ni have evidenced a high $E(2_1^+)$ energy [6] and a relatively small $B(E2; 0_{\text{gs}}^+ \rightarrow 2_1^+)$ value [7, 8], suggesting a large energy gap between between the pf shell and the $g_{9/2}$ orbital. However, the neutron separation energy shows no hints of magicity, which has prompted the suggestion that the low $B(E2; 0_{\text{gs}}^+ \rightarrow 2_1^+)$ value arises from a neutron dominated excitation and not from a shell closure [9]. Furthermore, well deformed structures have been observed at low excitations energies in ^{68}Ni which become the ground state in Fe and Cr isotopes.

Further studies on the $N = 40$ IoI below ^{68}Ni , as well as its possible extension towards $N = 50$, have been recently performed at the Radioactive Isotope Beam Factory (RIBF) of the RIKEN Nishina Center in Japan, largely with the use of the MINOS liquid hydrogen target [10] and the DALI2 [11] and DALI2⁺ [12] arrays for γ -ray detection. In this article, we review some recent experimental results on even- N isotopes around the $N = 40$ IoI, in particular using direct reactions with MINOS.

Section 2 presents the theoretical framework employed, while Sec. 3 describes the experimental setup. Results on even- and odd- Z isotopes are presented in Sec. 4 and 5, respectively. Future perspectives on the region are discussed in Sec. 6. More detailed reviews on shell evolution and the $N = 20$ and $N = 40$ Island of Inversion can be found in Refs.[4, 5, 13].

2 Theoretical approach

A remarkable shell model calculation which has been successfully used to explain most of the observable in this region is the one based on the Lenzi-Nowacki-Poves-Sieja (LNPS) interaction, which was published in 2010, ahead of many of the experimental results [14].

Previous theoretical studies reproduced early experimental information in the region, such as the level schemes of $^{62,64}\text{Fe}$, by using a realistic interaction and a valence space including the pf shells for protons and the $0f_{5/2}$, $1p_{3/2}$, $1p_{1/2}$, and $0g_{9/2}$ orbits for neutrons [15]. However, such calculations were not successful in making predictions towards heavier isotopes, with the necessity of including the $2d_{5/2}$ orbital pointed out [16]. This necessity arises from the fact that in the inclusion of the quasi-SU(3) sequence $0g_{9/2}$, $1d_{5/2}$, $2s_{1/2}$ together with the pseudo-SU(3) triplet $1p_{3/2}$, $0f_{5/2}$, $1p_{1/2}$ allows the development of quadrupole correlations which results in deformation [5].

The LNPS interaction is based on realistic two-body matrix elements with experimental constrains used to tune the monopole Hamiltonian. A model space based on a ^{48}Ca core, the pf shell for protons and the $1p_{3/2}$, $1p_{1/2}$, $0f_{5/2}$, $0g_{9/2}$, and $1d_{5/2}$ orbits for neutrons is adopted. As the third member of the quasi-SU(3) sequence, $2s_{1/2}$, is not included, its effect is compensated by an increase of the quadrupole-quadrupole interaction of the $0g_{9/2}$, and $1d_{5/2}$ orbits. Minor modifications to the monopole and pairing parts of the Hamiltonian have been included along the years to allow the description of a broader region. Although in some publications such modified interaction is referred as LNPS-m or LNPS-new, within this document the term LNPS will be used to refer to any version of the original interaction.

Figure 1 shows the neutron effective single particle energies (ESPE) of the LNPS interaction where a reduction of the $0f_{5/2} - 0g_{9/2}$ gap below ^{68}Ni is observed. Furthermore it can be seen that there is a very narrow separation between the $0g_{9/2}$ and the $1d_{5/2}$ orbits.

The calculation predicts a maximum on the deformation for ^{64}Cr , with the lowest $E(2_1^+)$ and the highest $B(E2; 0_{\text{gs}}^+ \rightarrow 2_1^+)$ value. For ^{68}Ni the wave function contains a large component corresponding to spherical configuration, although the occupation of the $0g_{9/2}$ is already visible and keeps increasing, as well as the occupation of the $1d_{5/2}$, when protons are removed. Regarding the ground state wave function, the 4p-4h component is dominant for Fe, Cr and Ti, although the 2p-2h and 6p-6h components are not negligible. This result is in contrast to the case of the $N = 20$ IoI, where the 2p-2h components dominates the ground state wave function. For ^{60}Ca , the LNPS calculation predicts a $E(2_1^+)$ of around 1.5 MeV. This increase in energy as compared to Ti, however, does not imply a double-magic character. The ground state wave function has more than three neutrons above the $N = 40$ gap,

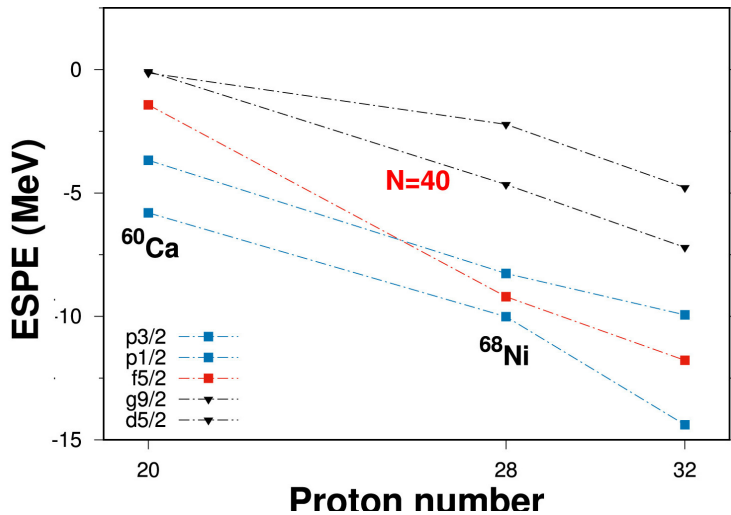


Fig. 1 Neutron effective single particle energies at $N = 40$ from the LNPS interaction. Reprinted from [5] with permission from ELSEVIER.

and only a 5% component from the doubly-magic configuration which place it within the IoI [14, 17].

The shell model calculations using the LNPS interaction provide a consistent framework to study the formation of an IoI at $N = 40$, which extends down to ⁶⁰Ca. It is noted that this situation, where deformed intruder states become energetically favoured, is described as due to the interplay between the presence of valence protons in the normal configuration and the reduction of the $N = 40$ gap approaching $Z = 20$.

3 Experimental approach

In recent years quasi-free scattering (QFS) and knockout reactions in inverse kinematics have been the preferred tools to measure isotopes very far from the valley of stability. Such direct reactions have the advantage of a high selectivity to probe individual nuclear orbitals, and offer the possibility to obtain information on angular momentum of the removed nucleon by measuring the momentum distribution of the residual fragment.

Exotic $N = 40$ isotones below ⁶⁸Ni have been measured at different facilities using a plethora of techniques [5, 13]. However, due to the low production cross section, reaching the most exotic species requires an increasingly high beam intensity. In the last decade, the combination of the highest primary beam intensities provided by the RIBF, with the MINOS liquid hydrogen target [10] has provided a significant amount of new information on exotic nuclei. In particular, by surrounding MINOS with the DALI2 and DALI2⁺ arrays [11, 12] the

structure of the most exotic neutron-rich isotopes could be investigated within the SEASTAR project [18].

Isotopes around the $N = 40$ IoI were produced during the SEASTAR 1 and SEASTAR 3 campaigns carried out in 2014 and 2017, respectively. Primary beams of ^{238}U and ^{70}Zn , with intensities of 12 and 240 pnA, respectively were used to produce the isotopes of interest, which were separated and identified with the BigRIPS separator [19]. For the case of SEASTAR 1 outgoing fragments were identified with the ZeroDegree spectrometer [19] and γ -rays were detected with the DALI2 array composed of 186 NaI(Tl) detectors [11], while for SEASTAR 3, the SAMURAI magnet [20] was used for the outgoing particle identification and the upgraded DALI2⁺ array consisting of 226 NaI(Tl) crystals [12] was used for γ -ray detection.

The use of the liquid hydrogen target of MINOS allowed to increase the luminosity and to reduce the background for secondary reactions. Target thicknesses of 100 and 150 mm were used for SEASTAR 1 and SEASTAR 3, respectively. The use of the time projection chamber which surrounds the target is indispensable to reconstruct the reaction-vertex position and improve the energy resolution obtained after Doppler correction. For the case of the MINOS target, it was possible to reconstruct the vertex position with a resolution of 5 mm FWHM [21].

4 The even- Z isotopes

4.1 *Fe isotopes*

As displayed in Fig. 2, the $E(2_1^+)$ and $E(4_1^+)$ of $^{64,66}\text{Fe}$ ($N = 38, 40$) show a significant decrease as compared to lighter Fe isotopes, indicating an increase of collectivity when approaching $N = 40$ [22]. Such conclusion has been supported by the measured transition probabilities in ^{66}Fe [23, 24]. Going beyond $N = 40$, the $E(2_1^+)$ of ^{68}Fe is only slightly reduced as compared to ^{66}Fe [25], while a modest increase on the $B(E2; 0_{\text{gs}}^+ \rightarrow 2_1^+)$ was reported [24]. These results have been interpreted by shell model calculations with the LNPS interaction, which reproduce the data and indicate the importance of excitations to the $g_{9/2}$ and $d_{5/2}$ orbitals in the understanding of the structure of isotopes in the $N = 40$ IoI.

The first spectroscopy of ^{70}Fe has been measured at the RIBF via β -decay [26] as well as in-beam γ -ray spectroscopy [21]. The latter measurement, which was the first published result of the SEASTAR project, also obtained the first spectroscopy of ^{72}Fe . In the experiment, excited states of $^{70,72}\text{Fe}$ and ^{66}Cr were populated by $(p, 2p)$ and $(p, 3p)$ reactions in MINOS. Two transitions were clearly visible in the DALI2 spectra corresponding to each isotope and, assigned to the decay of the 2_1^+ and 4_1^+ states based on the measured intensities, coincidence

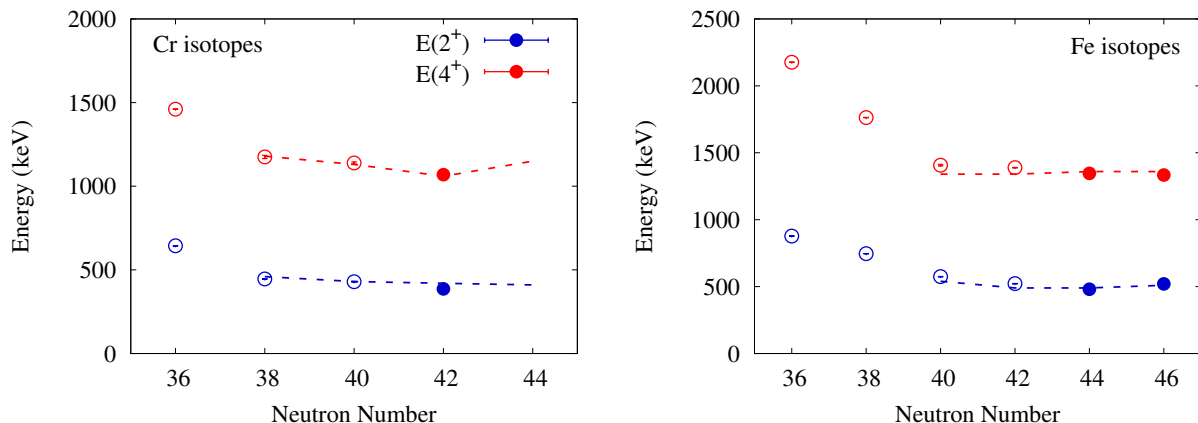


Fig. 2 Systematics of experimental $E(2_1^+)$ and $E(4_1^+)$ for Cr (left) and Fe (right) isotopes. Open circles represent previous literature values, while the filled squares indicate the results obtained within the SEASTAR project. Theoretical calculations with the LNPS interaction are shown by the dashed lines. Values taken from Ref. [21].

analysis, and systematic. The results are displayed in Fig. 2, where it can be seen that the measured $E(2_1^+)$ and $E(4_1^+)$ along the Fe isotopes show a seemingly constant value between $N = 40$ and $N = 46$, suggesting that there is no further increase of the deformation beyond $N = 40$ and that these isotopes remain within the $N = 40$ IoI and extend it towards $N = 50$.

Shell model calculations employing the LNPS interaction in the pf model space for protons and the $p_{1/2}f_{5/2}g_{9/2}d_{5/2}$ for neutrons reproduce the measurements successfully, as shown by the dashed lines in Fig. 2, and suggest that the neutron-rich Fe isotopes behave as prolate deformed rotational nuclei.

More recent spectroscopic measurements on ^{70}Fe using the high-resolution Ge array GREINA [27, 28] following proton removal reactions, have reported in addition a candidate for the 6^+ state at 2444 keV, as well as effective lifetimes of $\tau = 120(20)$ ps and $\tau = 2.3(1.5)$ ps for the 2_1^+ and 4_1^+ states, respectively [29]. Although these lifetime values represent an upper limit due to possible unobserved feeding, a general good agreement with the LNPS calculations is observed. Furthermore, the calculations place the 6^+ state within 30 keV of the experimental value, showing their remarkable predictive capabilities.

4.2 Cr isotopes

In a similar way as for the Fe isotopes, for the Cr isotopic chain a strong deformation when reaching $N = 40$ was suggested. These conclusions were based on previous measurements of the $E(2_1^+)$ of $^{62,64}\text{Cr}$ ($N = 38, 40$) [15, 30], and supported by the measurements of transition

probabilities [31, 32]. Furthermore, a recent study on ^{62}Cr reported for the first time an excited 0^+ state, revealing shape coexistence in this region [33].

Beyond $N = 40$, ^{66}Cr is the heaviest Cr isotope for which spectroscopic information is available. The measurement was performed within the SEASTAR project, together with the Fe isotopes as described above. Two transitions were observed in the γ -ray spectrum measured with DALI2 following quasi-free proton knockout, and assigned to the 2_1^+ and 4_1^+ states of ^{66}Cr . Figure 2 displays the obtained results together with the systematics of $E(2_1^+)$ and $E(4_1^+)$ of lighter Cr isotopes. It can be seen that the Cr isotopes follow a similar trend as the Fe isotopes with the $E(2_1^+)$ and $E(4_1^+)$ remaining constant from $N = 38$ to $N = 42$, and with ^{66}Cr showing the lowest $E(2_1^+)$ in the region at 386 keV, slightly below the value of ^{64}Cr of 429 keV.

Shell model calculation using the LNPS interaction reproduce the experimental data, as shown by the dashed lines in Fig. 2. The calculations show that the deformation stays constant, with a maximum at $N = 40$ where an intrinsic shape with deformation parameter $\beta \sim 0.33$ arises resulting in the constant energy values. Despite this, a varying degree of particle-hole excitations across $N = 40$ is predicted along the isotopic chain [21].

Further shell model calculations considering the pf shell for protons and the sdg shell for neutrons and a ^{60}Ca core, have been performed to study the evolution of the $N = 40$ Island of Inversion towards $N = 50$. An effective interaction containing some modifications to the LNPS interaction and termed PFSDG-U has been employed [17]. Such calculations also highlight the interplay between quadrupole and pairing correlations and predict a merging of the $N = 40$ IoI with a new one formed around $N = 50$, in a similar way as the $N = 20$ IoI continues towards $N = 28$.

4.3 Ti isotopes

Experimental information for Ti isotopes around $N = 40$ is limited. Early measurements on production cross sections from the fragmentation of a ^{76}Ge beam indicated that the $Z = 19 - 22$ neutron-rich nuclei display an enhanced cross section with respect to the lighter isotopes and turned to be more bound than predicted by mass models [34].

The first spectroscopy of ^{60}Ti , measured at NSCL with the GREYINA array, showed $2_1^+ \rightarrow 0_{\text{gs}}^+$ and $4_1^+ \rightarrow 2_1^+$ transition energies of 850(5) and 866(5) keV, respectively [35]. Shell model calculations both with and without including the $g_{9/2}$ orbital were able to reproduce the observed excited states. However, only the calculation including excitations above $N = 40$ could successfully reproduce the measured knockout cross sections.

Isomer spectroscopy has revealed two new isomers in ^{61}Ti [36]. Comparison of this result with shell model calculations based on the LNPS interaction suggested that particle-hole

excitations across $N = 40$ dominate the ground state configurations of $^{59,61}\text{Ti}$, placing them within the $N = 40$ IoI.

Recent mass measurements on Sc, V and Ti isotopes using the time-of-flight method show that the two-neutron separation energy, S_{2n} , is flat for the Ti isotopes when going towards $N = 40$, indicating that they are more stable than expected [37].

Obtaining spectroscopic information along the $N = 40$ isotones when going from ^{64}Cr to the lighter even- Z isotope, namely ^{62}Ti , took 10 years and could only be achieved at the RIBF within the SEASTAR project. In the experiment, ^{62}Ti was populated by proton knockout reactions from ^{63}V in the MINOS target. γ -ray spectroscopy performed with the DALI2⁺ array showed two transitions at 683(10) and 823(20) keV tentatively assigned to the decays of the 2_1^+ and 4_1^+ states, respectively [38]. Comparison with theoretical predictions based on the LNPS interaction, performed already in 2010, is exceptionally good as can be seen in Fig. 3 where the known experimental $E(2_1^+)$ and $E(4_1^+)$ of even-even $N = 40$ isotones are compared to these calculations. Within this theoretical framework the ground state of ^{62}Ti is dominated by 4p-4h excitations with a significant component of 6p-6h resulting from a gap of about 1 MeV between the $f_{5/2}$ and the $g_{9/2}$. This result places ^{62}Ti within the $N = 40$ IoI and suggests that it extends to ^{60}Ca .

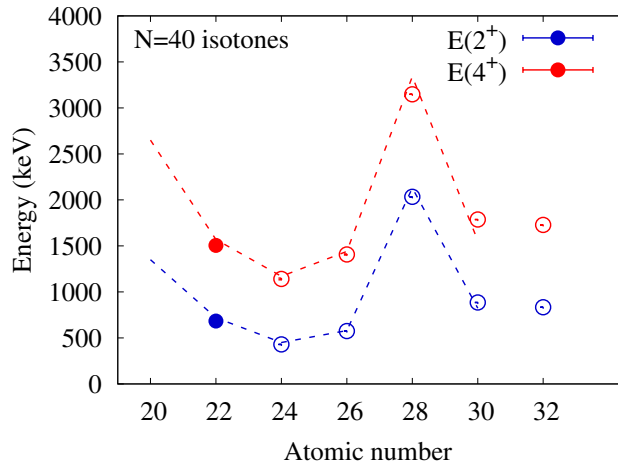


Fig. 3 $E(2_1^+)$ and $E(4_1^+)$ of even-even $N = 40$ isotones. Available experimental data is compared with the results of shell model calculations using the LNPS interaction, shown by the dashed lines. The filled circles indicate the results obtained within the SEASTAR project. Values taken from Ref. [38].

4.4 Ca isotopes

For the Ca isotopic chain towards $N = 40$, spectroscopic information of $^{56,58}\text{Ca}$, beyond the proposed $N = 34$ shell closure, has been measured for the first time within the SEASTAR project by proton knockout reactions off $^{57,59}\text{Sc}$ in the MINOS target. In ^{56}Ca a γ -ray transition was detected at 1456(12) keV, while in ^{58}Ca , a possible transition at 1115(34) keV was observed with a significance of 2.8σ . Both transitions were attributed to the decay of the 2_1^+ state in the corresponding Ca isotopes [39].

For Ca isotopes up to ^{54}Ca ($N = 34$), a good agreement has been obtained with shell model calculations employing the GXPF1 family of interactions [40–42]. In these calculations, the consideration of the full pf shell is sufficient to reproduce the energies of lying states, and reproduce the $E(2_1^+)$ at the $N = 32$ and $N = 34$ sub-shell closures. Within the same model, the $E(2_1^+)$ of $^{56,58}\text{Ca}$ should remain constant. The experimentally observed reduction of excitation energy when going from $N = 36$ to $N = 38$ suggest that the $f_{5/2}$ does not behave like an isolated orbital but instead couples to the $g_{9/2}$ orbital, preventing the formation of an $N = 40$ gap around ^{60}Ca . Shell model calculations with the A3DA-m interaction, fitted to reproduce the experimental data, suggest a pairing between these two orbitals with a consequential prediction of the drip line in Ca isotopes at $N = 50$ [39, 43].

Spectroscopic information on odd- A Ca isotopes was also obtained within the SEASTAR project. The measurement of a short-lived state in ^{57}Ca at 751(13) keV suggests a structural change at $N = 36$ where the particle-hole configurations are dominant, in agreement with the development of the $N = 40$ Island of Inversion [44]. Further information on the structure of the Ca isotopes recently obtained at the RIBF can be found elsewhere [45].

The discovery of the $N = 40$ isotope of Ca, namely ^{60}Ca , from the fragmentation of a ^{70}Zn beam at the RIBF has been only recently reported [46]. Although spectroscopy of ^{60}Ca cannot be achieved at the existing facilities, it will become accessible after the planned upgrade of the RIBF [47]. Based on the good agreement between the different experimental measurements, in particular the spectroscopy of ^{62}Ti , with the LNPS calculations, an $E(2_1^+)$ or around 1.5 MeV is to be expected, followed by a triplet of 0^+ , 2^+ and 4^+ states [5].

5 The odd- Z isotopes

5.1 Co isotopes

The Co isotopic chain, with only one proton hole below the magic $Z = 28$, has been the subject of extensive research as nuclei with only one particle or hole outside of a magic shell closure allow to study the interplay between the collective and single-particle degrees of

freedom, and to investigate the strength of the shell gaps. Indeed, the structure of Co isotopes up to $N = 38$ is well described by the coupling of the $\pi f_{7/2}^{-1}$ proton hole to its adjacent Ni isotope, asserting the conservation of the $Z = 28$ gap.

The discovery of a $1/2^-$ isomeric state in ^{67}Co with a surprisingly low energy of 492 keV [48] was interpreted within the Nilsson model as a collective structure at $N = 40$ arising from an intruder state. Furthermore, the $3/2^-$ and $5/2^-$ states were suggested to belong to a rotational band on top of this deformed structure. On the other hand, the measured $9/2^-$ and $11/2^-$ states followed the systematic of lighter Co isotopes and could be interpreted as the core-coupled states. Such a discovery pointed at shape coexistence when reaching the Ni isotopes. Further information on the structure towards ^{78}Ni , studied within the SEASTAR project, can be found elsewhere [49].

The structure of ^{65}Co , at $N = 38$, showed similar features, which was interpreted as arising from the influence of the deformed intruder configuration, although not as well developed as in ^{67}Co [50]. By using shell model calculations with large model spaces and, in particular, the LNPS interaction, a simultaneous description of both the core-coupled and the deformed structures up to ^{67}Co was possible, showing the importance of including the $g_{9/2}$ and $d_{5/2}$ orbitals to account for the deformed configurations [51].

For the case of ^{69}Co , β -decay studies have reported few γ -ray transition, which, however, could not be placed in a level scheme [52]. The presence of a 750(250) ms β -decaying isomer was also reported and suggested to correspond to the $1/2^-$ deformed state similar to the ones observed in $^{65,67}\text{Co}$. Only recently the excitation energy of this isomer has been reported to be 176(57) keV, indicating the persistence of shape coexistence in the region [53].

Spectroscopic information of Co isotopes beyond $N = 40$ has been accessible within the SEASTAR project. Excited states in $^{69,71,73}\text{Co}$ were populated by proton knockout reactions on $^{70,72,74}\text{Ni}$ and their de-excitation γ -rays measured with the DALI2 array [54]. Level schemes for the three isotopes were proposed based on the $\gamma - \gamma$ coincidence analysis. In order to assign the spin of the measured levels, shell model calculations were performed. For $^{69,71}\text{Co}$, the $pf_{5/2}g_{9/2}d_{5/2}$ model space together the LNPS interaction was employed, while for ^{73}Co the $pf - sdg$ model space and the PFSDG-U interaction was used. Based on the agreement of the calculations with the experimental level schemes, candidates for the $9/2^-$ and $7/2^-$ states in each isotope were proposed. Figure 4 shows the experimental level schemes as well as the theoretical calculations for $^{69,71,73}\text{Co}$. As a comparison, the $E(2_1^+)$ of the neighboring Ni isotopes are also displayed as a green dashed line. It can be seen that the $9/2^-$ state follows the trend of the $E(2_1^+)$, suggesting that core coupling is maintained in this region.

The calculations predict that, in addition to this spherical structure based on the $\pi f_{7/2}^{-1} \otimes 2^+(\text{Ni})$, a coexisting band with a deformed structure based on a $\pi f_{7/2}^{-2} p f^{+1}$ configuration exists, similarly as for the lighter Co isotopes. Although low energy transitions were measured during the SEASTAR experiment, the placement of such a deformed structure could not be determined.

Interestingly, the measurement of the β -decay of ^{75}Co performed at the RIBF using the EURICA setup, revealed the presence of an isomeric transition at 1914(2) keV with a proposed $J^\pi = (1/2^-)$ spin and parity assignment [55]. This state differs by about 1 MeV from the shell model prediction, which assign this state as a prolate deformed state. A clear understanding on shape coexistence along the Co isotopic chain requires further investigation.

5.2 Mn isotopes

For the mid-shell isotopes Mn and V, spectroscopic information is very limited due to the high level density and their sensitivity to both the single-particle and collective degrees of freedom, which leads to a diversity of structures at low excitation energies. Studying these isotopes offers additional insights into shell evolution, while also providing robust means of testing the effectiveness of interactions developed for this particular region of the nuclear chart.

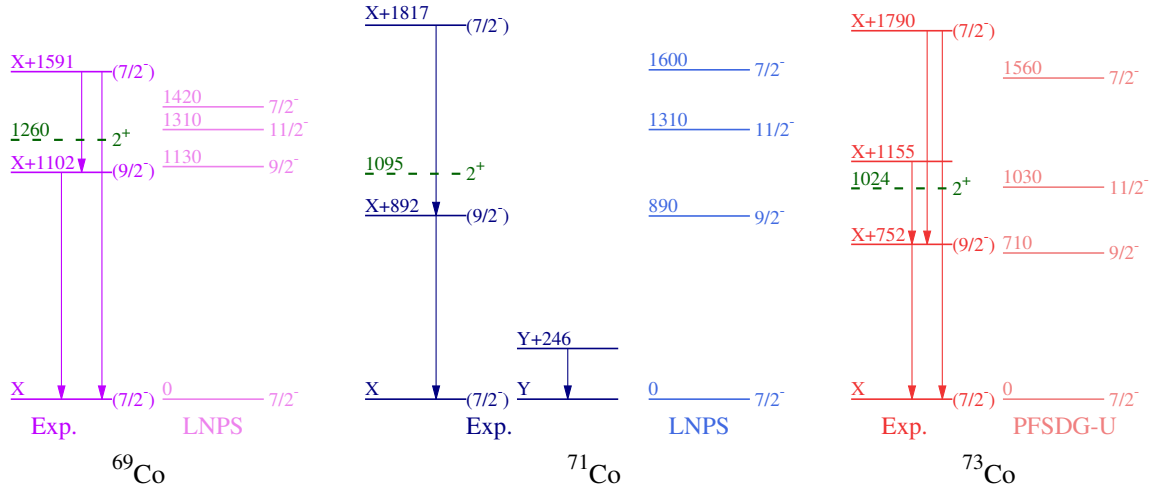


Fig. 4 Experimental level schemes of $^{69,71,73}\text{Co}$ and comparison with theoretical calculations with the LNPS and PFSDG-U interactions. For comparison the 2_1^+ state of the corresponding Ni isotopes are displayed by the green dashed lines. Values taken from [54]

For ^{63}Mn , the heaviest Mn isotope with a level scheme reported prior to the SEASTAR campaigns, the $7/2^-$, $9/2^-$, and $11/2^-$ excited states were measured and compared to shell model calculations using the LNPS interaction and various model spaces. Based on such a comparison it was established that the calculation with the model space consisting of the fp shell for protons and the $pf_{5/2}g_{9/2}d_{5/2}$ orbitals for neutrons, provided the best agreement with the experimental data [56]. Furthermore, the calculations indicated that the low-lying structure of ^{63}Mn presents a significant mixing of the proton configurations, unlike in the simple single-particle approximation, where the structure would be dominated by a three $f_{7/2}$ proton holes configuration. This necessity to include the $\nu g_{9/2}$ and $\nu d_{5/2}$ in lighter Mn isotopes had been pointed out by previous spectroscopy studies [57, 58], as well as by measurements of quadrupole moments [59–61].

During the SEASTAR 1 campaign, the neutron-rich $^{63,65,67}\text{Mn}$ isotopes were produced by the fragmentation of ^{68}Fe via the $^{68}\text{Fe}(p, 2pxn)^{67-x}\text{Mn}$ reactions with $x = 4, 2, 0$, respectively. Level schemes for the three isotopes were deduced based on the coincidence analysis and the systematics in the region [62]. Similarly to the lighter isotopes, a sequence of $7/2^-$, $9/2^-$, and $11/2^-$ excited states on top of the suggested ($5/2^-$) ground state was proposed.

Figure 5a) shows the evolution of low-lying states along the Mn isotopes. Shell model calculations using the LNPS interaction are shown by the dashed lines. It can be seen that the theoretical calculations give good account of the experimental results, in particular the decrease on the energies of the $9/2^-$ and $11/2^-$ states in $^{65,67}\text{Mn}$. The wave function of $^{63,65,67}\text{Mn}$ results to be dominated by $4p - 4h$ neutron excitations to the $g_{9/2}$ and $d_{5/2}$ orbitals beyond the $N = 40$ shell gap. In addition, the calculation suggest that the $7/2^-$, $9/2^-$, and $11/2^-$ states belong to a rotational band with $K = 5/2$.

By plotting the excitation energy of the states as a function of $J(J + 1)$, as shown in Fig. 5b), the characteristics of a rotational band can be observed. For $N = 40$ and $N = 42$ a fairly linear relationship is present, showing a behaviour consistent with textbook rotational bands. Below $N = 40$, some degree of non-linearity is present, showing a possibility of a triaxial deformation, or a softness of the potential, as already proposed for ^{63}Mn [61], indicating an evolution towards strong coupling along the isotopic chain.

5.3 V isotopes

Spectroscopic information on V isotopes is even more scarce than for Mn isotopes, with ^{57}V being the last even- N isotope which had available information prior to the SEASTAR campaigns. For this isotope, a candidate for the $11/2^-$ state has been reported at 1.163 MeV based on γ -ray spectroscopy following multinucleon transfer reactions [63]. Additionally, few states at excitation energies below 200 keV, as well as a group of states at around 1.7 MeV

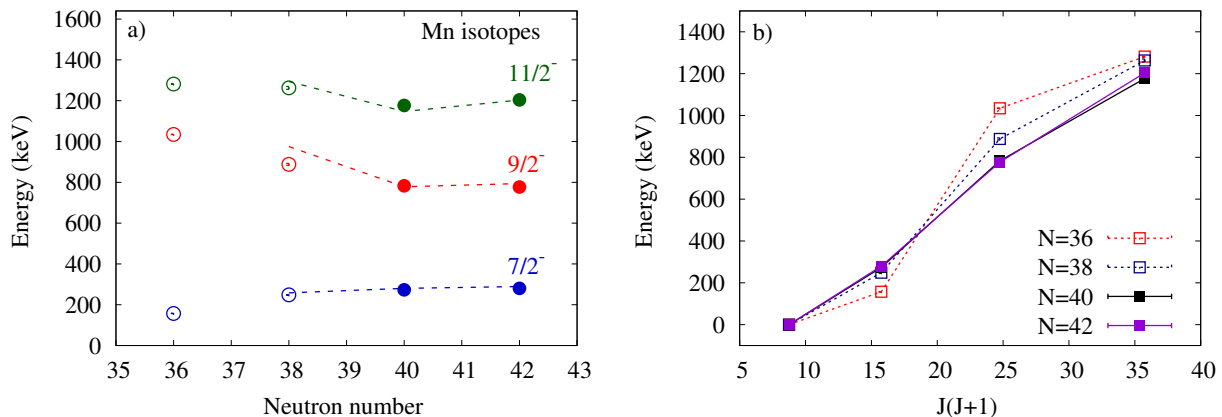


Fig. 5 a) Evolution of low lying $7/2^-$, $9/2^-$ and $7/2^-$ states in Mn isotopes. Shell model calculations with the LNPS interaction are shown by the dashed lines. b) Energy of the low lying states in Mn isotopes as a function of $J(J+1)$. Adapted from [62].

have been measured following the β -decay of ^{57}Ti [64]. Shell model calculations employing the GXPF1A interaction in the pf -shell model space gave a moderate agreement with the experimental data and suggested that the triplet of low-energy states could correspond to the $7/2^-$, $5/2^-$, and $3/2^-$ states, favoring the $7/2^-$ assignment for the ground state.

Spectroscopic information on $^{59,61,63}\text{V}$ was obtained for the first time during the SEASTAR 3 campaign. Due to the limited acceptance of the SAMURAI spectrometer for these isotopes, low statistics were obtained and different reactions had to be employed to populate excited states: For ^{59}V the two-neutron knockout reaction provided enough statistics to identify four γ -ray transitions in the γ -ray spectrum. In the case of ^{61}V , neutron knockout and, with lower statistics, inelastic proton scattering were employed revealing five transitions [65]. Finally, in ^{63}V mainly contributions from proton knockout and inelastic scattering were employed and only two γ rays were measured with a confidence level above 3σ [66]. Due to the limited statistics, only in the case of ^{61}V a coincidence analysis was possible, establishing coincidences between some of the observed transitions [65].

Aiming to place the observed γ -rays in a level scheme, shell model calculations with the LNPS interaction were performed. The results of the calculations can be seen in Fig. 6. In the three cases, two different sets of states are proposed, resembling the situation of ^{57}V : At low excitation energies, below 400 keV, the $3/2^-$, $5/2^-$ and $7/2^-$ states are located. At higher excitation energies of around 1 MeV, the $9/2^-$ and $11/2^-$ states are predicted. According to the same calculation, the ground state of $^{61,63}\text{V}$ is predicted to be the $3/2^-$, while for ^{59}V , where the three levels lie within 100 keV, the $5/2^-$ is suggested as the ground state.

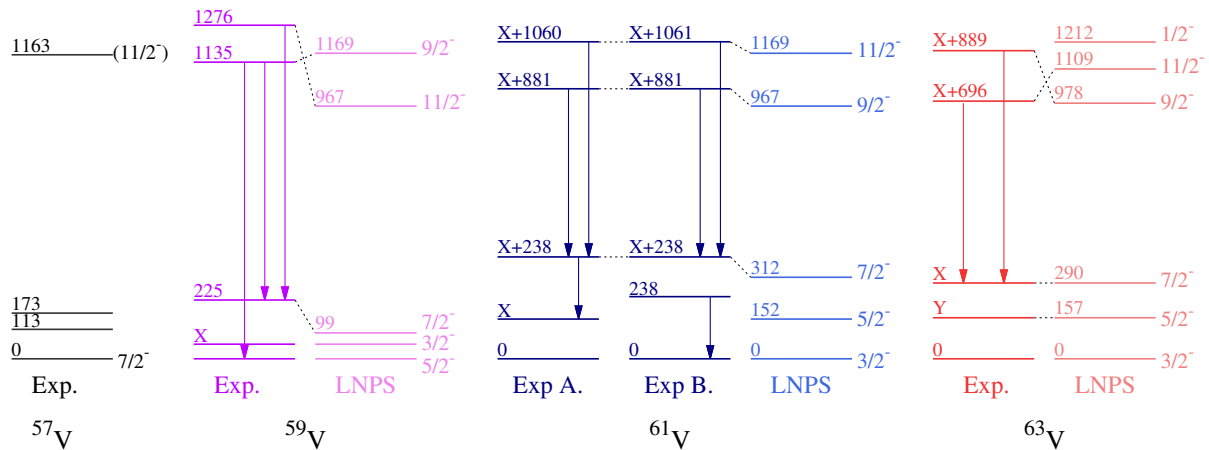


Fig. 6 Experimental level schemes of neutron-rich $^{57,59,61,63}\text{V}$ [63–66]. For $^{59,61,63}\text{V}$ the experimental level schemes are compared with shell model calculations with the LNPS interaction.

For the case of ^{59}V [65], the measured γ -ray energies are in better agreement with the decay of the $9/2^-$ and $7/2^-$ states. Based on this, and on the comparison between the theoretical branching ratios and the experimental intensities, three of the measured γ -rays were assigned to the level scheme, as shown in Fig. 6. A similar argument can be applied for the cases of $^{61,63}\text{V}$ [65, 66]. In these cases the experimental (p, p') cross sections were compared with coupled channels calculations assuming an axially symmetric rotor model. While predicted cross sections to the low-lying $3/2^-$, $5/2^-$ and $7/2^-$ states are much larger than the measured ones, a consistency was found for the population of the $9/2^-$ and $11/2^-$ states, strengthening the proposed spin and parity assignments and allowing to construct the level schemes shown in Fig. 6. It is noted that due to the high atomic background present in the experiment, it was not possible to measure low-energy transition, which leads to an ambiguity on the level scheme. Because of this, for ^{61}V two possible levels schemes have been proposed, as shown in Fig. 6.

The (p, p') reaction on $^{61,63}\text{V}$ was further exploited by the comparison of the measured cross sections with coupled channels calculations assuming only a quadrupole deformation, as well including an hexadecapole contribution. Although for ^{61}V no firm conclusion was possible, for ^{63}V deformation parameters of $\beta_2 = 0.24(2)$ and $\beta_4 = 0.08(1)$ were obtained, indicating that this $N = 40$ isotope belongs to the Island of Inversion.

5.4 Sc isotopes

The Sc isotopes, with a single valence proton above the Ca isotopes, are an ideal testing ground for the study of neutron excitation in the pf shell in the presence of an odd proton, as well as to the coupling of this valence proton with the Ca core. Indeed, in a shell-model picture, the coupling of the valence $f_{7/2}$ proton with the 2_1^+ state of the Ca core would lead to multiplet of five states with spin and parity of $11/2^-$, $9/2^-$, $7/2^-$, $5/2^-$, and $3/2^-$.

For ^{53}Sc ($N = 32$), excited states have been measured following multinucleon transfer reactions [67]. Transitions at 2283, 345, and 2616 keV were measured to depopulate two states at 2.3 and 2.6 MeV. The proposed level scheme showed a good agreement with shell model calculations in the pf shell employing the UPF and GXPF1A interactions, and suggested that these two levels correspond to the $9/2^-$ and $11/2^-$ states, belonging to the multiplet arising from the coupling of the valence proton with the ^{52}Ca core. A candidate for the $3/2^-$ state at 2.1 MeV has been identified from β -decay studies [68, 69] as well as from proton knockout [70]. Interestingly, in the proton knockout reaction the proposed $9/2^-$ and $11/2^-$ states were not observed, which is consistent with the proton knockout populating preferentially proton-hole states.

The heaviest even- N Sc isotope where spectroscopic information is available is ^{55}Sc , located just above the recently established $N = 34$ sub-shell closure. Low lying states on ^{55}Sc were populated by proton knockout reaction and inelastic scattering, and based on coincidences analysis a level scheme was proposed and compared with shell model calculations using the SDPF-MU interaction, and with *ab-initio* calculations. Based on the good agreement with the calculations, a candidate for the $3/2^-$ state was proposed at 695 keV. As no significant increase on the energy of this state was observed, unlike for the Ca isotopes, it was concluded that there is no significant $N = 34$ shell closure for Sc isotopes [71].

No spectroscopic information is yet available for Sc isotopes towards $N = 40$. Mass measurements for $^{55-60}\text{Sc}$ have been recently reported showing a continuous declining trend towards $N = 39$ [37]. For ^{61}Sc , only one proton above ^{60}Ca , although its existence has been reported [46], no spectroscopic information is available.

Detailed spectroscopy of ^{55}Sc as well as first spectroscopy of $^{57,59}\text{Sc}$ has also been achieved within the SEASTAR 3 campaign. Preliminary results of the analysis of ^{55}Sc show agreement with the low-lying structure previously reported [72], as well as a new transition at 1510 keV decaying directly to the ground state [73]. Further interpretation on these results, as well as the first spectroscopy of $^{57,59}\text{Sc}$ will be discussed elsewhere [74].

6 Future perspectives

Further investigation on the $N = 40$ Island of Inversion can help us build a consistent view of shell evolution in the region, and to test the existing theoretical models, aiming to consolidate a unified description of these nuclei.

On the side of the even-even isotopes, the first spectroscopy of ^{60}Ca would be a crucial milestone for the study of the $N = 40$ Island of Inversion. Only such a measurement can give direct evidence of this sub-shell closure for the Ca isotopes. Moreover, first spectroscopy of ^{64}Ti , beyond $N = 40$, can provide a strong benchmark for the theoretical models. However, as predicted by the shell model calculations with the LNPS interaction, in spite of the fact that the $E(2_1^+)$ for ^{60}Ca is expected to increase with respect to the neighbouring ^{62}Ti , a sizable shell gap at $N = 40$ is unlikely. Measurement of this gap can only be obtained by mass measurements in this region, which are, therefore, of fundamental importance. Furthermore, to study shell evolution beyond $N = 40$, as well as the merging of the $N = 40$ and $N = 50$ Islands of Inversion, spectroscopic measurements on $^{74,76}\text{Fe}$ are necessary.

In addition, to have direct information on the collectivity around $N = 40$ it is essential to measure transition probabilities. Lifetime measurements of $^{56,58}\text{Ti}$ via lineshape analysis have been recently performed at the RIBF employing high-resolution Ge detectors within the HiCARI project [75]. These results can be extended in the more exotic ^{60}Ti , as well as Cr and Fe isotopes.

For odd- Z isotopes, of particular importance are the measurements in Co isotopes, and specially the investigation on the low-lying $1/2^-$ states, which have indicated shape coexistence when going towards ^{78}Ni . Deeper exploration of this phenomenon requires the development of dedicated techniques to be able to measure the 0^+ states in neighbouring even-even isotopes.

Upcoming results on the Sc isotopes will shed light not only on the shell evolution towards $N = 40$ but also on the rapid changes observed for the $N = 32$ and $N = 34$ shell closures when adding a single valence proton. A comprehensive understanding of this region requires the development of shell model calculations which allow to include not only neutron excitations across $N = 40$ towards the $g_{9/2}$ and $d_{5/2}$ orbitals, but also the contribution from the excitations of protons from the sd shell. Such calculations are of particular importance in understanding the states observed following proton knockout reactions.

While some of these measurements are experimentally achievable at the RIBF with the current detectors, many others require significant upgrades both from the accelerator side, and the detection systems. The planned RIBF upgrade will achieve unprecedented beam intensities [47], which will in turn call for improvements on the detection systems. In

particular, for γ -ray spectroscopy, the development of the HYPATIA array will contribute significantly to spectroscopic studies of very neutron-rich nuclei, where an improved efficiency is necessary to effectively use the available beam time [76]. A review on the detector developments for next-generation quasi-free scattering can be found elsewhere [77].

7 Summary

Studies in shell evolution for exotic isotopes far from the valley of stability have revealed the appearance of new shell closures as well as the disappearance of some others. In particular for $N = 40$, which is a sub-shell closure arising from the harmonic oscillator potential, an IoI has been established, where deformed intruder configurations overtake the contribution of spherical configurations in the wave function.

Within the SEASTAR project, the high intensity beams provided by the RIBF have been efficiently exploited by the use of quasi-free reaction studies. The combination of the liquid hydrogen target of MINOS with the high-efficiency γ -ray detector arrays DALI2 and DALI2⁺ have been crucial to study shell evolution around the $N = 40$ IoI and its possible extension towards $N = 50$.

A variety of results, particularly related to γ -ray spectroscopy have been discussed. Measurements on $E(2_1^+)$ and $E(4_1^+)$ of even-even isotopes, as well as first spectroscopic studies of odd- Z isotopes have considerably increased the experimental information in this region. Likewise, inclusive and exclusive cross sections for direct reactions have been exploited to characterize the nature of the observed excited states.

Shell model calculations employing the LNPS interaction in a model space consisting of the pf shell for protons and the $1p_{3/2}$, $1p_{1/2}$, $0f_{5/2}$, $0g_{9/2}$, and $1d_{5/2}$ orbitals for neutrons has successfully reproduce the experimental data and has demonstrated a high prediction power regarding shell evolution in this region. These calculations also suggest exciting possibilities, such as the merging of the $N = 40$ and $N = 50$ Island of Inversion and shape coexistence.

Thanks to the upcoming upgrades on the RIBF accelerators and detection systems, as well as the next generation facilities FRIB and FAIR, further experimental studies on exotic isotopes will be within reach, which will help us understand the mechanisms governing shell evolution and the fundamental nuclear force.

Acknowledgment

I would like to thank all the speakers of the session devoted the the $N = 40$ Island of Inversion during the symposium on “Direct reactions and spectroscopy with hydrogen

targets: past 10 years at the RIBF and future prospects” held at York, UK in August 2023. I would like to specially acknowledge Silvia M. Lenzi, R. Taniuchi and S. Chen for the careful reading of this manuscript and the many useful comments and suggestions.

References

- [1] M. G. Mayer, *Phys. Rev.*, **75**, 1969–1970 (1949).
- [2] O. Haxel, J. H. D. Jensen, and H. E. Suess, *Phys. Rev.*, **75**, 1766–1766 (1949).
- [3] O. Sorlin and M.-G. Porquet, *Prog. Part. Nucl. Phys.*, **61**(2), 602–673 (2008).
- [4] T. Otsuka et al., *Rev. Mod. Phys.*, **92**, 015002 (2020).
- [5] F. Nowacki, A. Obertelli, and A. Poves, *Prog. Part. Nucl. Phys.*, **120**, 103866 (2021).
- [6] R. Broda et al., *Phys. Rev. Lett.*, **74**, 868–871 (1995).
- [7] O. Sorlin et al., *Phys. Rev. Lett.*, **88**, 092501 (2002).
- [8] N. Bree et al., *Phys. Rev. C*, **78**, 047301 (2008).
- [9] K. Langanke et al., *Phys. Rev. C*, **67**, 044314 (2003).
- [10] A. Obertelli et al., *Eur. Phys. J. A*, **50**, 8 (2014).
- [11] S. Takeuchi et al., *Nucl. Instrum. Methods Phys. Res. A*, **763**, 596 – 603 (2014).
- [12] I. Murray et al., *RIKEN Accel. Prog. Rep.*, **51**, 158 (2017).
- [13] A. Gade, *Physics*, **3**(4), 1226–1236 (2021).
- [14] S. M. Lenzi et al., *Phys. Rev. C*, **82**, 054301 (2010).
- [15] O. Sorlin et al., *Eur. Phys. J. A*, **16**(1), 55–61 (2003).
- [16] E. Caurier, F. Nowacki, and A. Poves, *Eur. Phys. J. A*, **15**(1), 145–150 (2002).
- [17] F. Nowacki et al., *Phys. Rev. Lett.*, **117**, 272501 (2016).
- [18] The SEASTAR project, <https://www.nishina.riken.jp/collaboration/SUNFLOWER/experiment/seastar/index.php> (2024).
- [19] T. Kubo et al., *Progr. Theor. Exp. Phys.*, **2012**(1) (2012).
- [20] T. Kobayashi et al., *Nucl. Instrum. Methods Phys. Res. B*, **317**, 294–304 (2013).
- [21] C. Santamaria et al., *Phys. Rev. Lett.*, **115**, 192501 (2015).
- [22] M. Hannawald et al., *Phys. Rev. Lett.*, **82**, 1391–1394 (1999).
- [23] W. Rother et al., *Phys. Rev. Lett.*, **106**, 022502 (2011).
- [24] H. L. Crawford et al., *Phys. Rev. Lett.*, **110**, 242701 (2013).
- [25] P. Adrich et al., *Phys. Rev. C*, **77**, 054306 (2008).
- [26] G. Benzoni et al., *Phys. Lett. B*, **751**, 107–112 (2015).
- [27] S. Paschalis et al., *Nucl. Instrum. Methods Phys. Res. A*, **709**, 44–55 (2013).
- [28] D. Weisshaar et al., *Nucl. Instrum. Methods Phys. Res. A*, **847**, 187–198 (2017).
- [29] A. Gade et al., *Phys. Rev. C*, **99**, 011301 (2019).
- [30] A. Gade et al., *Phys. Rev. C*, **81**, 051304 (2010).
- [31] N. Aoi et al., *Phys. Rev. Lett.*, **102**, 012502 (2009).
- [32] T. Baugher et al., *Phys. Rev. C*, **86**, 011305 (2012).
- [33] Alexandra Gade et al., *Nature Physics* (Oct 2024).
- [34] O. B. Tarasov et al., *Phys. Rev. Lett.*, **102**, 142501 (2009).
- [35] A. Gade et al., *Phys. Rev. Lett.*, **112**, 112503 (2014).
- [36] K. Wimmer et al., *Phys. Lett. B*, **792**, 16–20 (2019).
- [37] S. Michimasa et al., *Phys. Rev. Lett.*, **125**, 122501 (2020).
- [38] M. L. Cortés et al., *Phys. Lett. B*, **800**, 135071 (2020).
- [39] S. Chen et al., *Phys. Lett. B*, **843**, 138025 (2023).
- [40] M. Honma et al., *Eur. Phys. J. A*, **25**(1), 499–502 (2005).
- [41] D. Steppenbeck et al., *Nature*, **502**(7470), 207–210 (2013).
- [42] S. Chen et al., *Phys. Rev. Lett.*, **123**, 142501 (2019).
- [43] T. Tsunoda, Y. Otsuka, N. Shimizu, M. Honma, and Y. Utsuno, *Phys. Rev. C*, **89**, 031301 (2014).
- [44] T. Koiwai et al., *Phys. Lett. B*, **827**, 136953 (2022).
- [45] H. Liu, S. Chen, and F. Browne, Shell migration at N=32,34 around Ca region (2024), In this volume.
- [46] O. B. Tarasov et al., *Phys. Rev. Lett.*, **121**, 022501 (2018).
- [47] RIBF Facility Upgrade Project, https://www.nishina.riken.jp/researcher/RIBFupgrade/index_e.html (2024).
- [48] D. Pauwels et al., *Phys. Rev. C*, **78**, 041307 (2008).
- [49] R. Taniuchi, Competition of the shell closure and deformations across the doubly magic 78ni (2024), In this

volume.

- [50] D. Pauwels et al., Phys. Rev. C, **79**, 044309 (2009).
- [51] F. Recchia et al., Phys. Rev. C, **85**, 064305 (2012).
- [52] S. N. Liddick et al., Phys. Rev. C, **92**, 024319 (2015).
- [53] L. Canete et al., Phys. Rev. C, **101**, 041304 (2020).
- [54] T. Lokotko et al., Phys. Rev. C, **101**, 034314 (2020).
- [55] S. Escrig et al., Phys. Rev. C, **103**, 064328 (2021).
- [56] T. Baugher et al., Phys. Rev. C, **93**, 014313 (2016).
- [57] J. J. Valiente-Dobón et al., Phys. Rev. C, **78**, 024302 (2008).
- [58] C. J. Chiara et al., Phys. Rev. C, **82**, 054313 (2010).
- [59] C. Babcock et al., Phys. Lett. B, **750**, 176–180 (2015).
- [60] C. Babcock et al., Phys. Lett. B, **760**, 387–392 (2016).
- [61] H. Heylen et al., Phys. Rev. C, **94**, 054321 (2016).
- [62] X. Y. Liu et al., Phys. Lett. B, **784**, 392–396 (2018).
- [63] S. Lunardi, AIP Conf. Proc., **1072**(1), 160–165 (2008).
- [64] S. N. Liddick et al., Phys. Rev. C, **72**, 054321 (2005).
- [65] Z. Elekes et al., Phys. Rev. C, **106**, 064321 (2022).
- [66] M. M. Juhász et al., Phys. Rev. C, **103**, 064308 (2021).
- [67] S. Bhattacharyya et al., Phys. Rev. C, **79**, 014313 (2009).
- [68] H. L. Crawford et al., Acta Phys. Pol. B, **40**, 481 (2009).
- [69] H. L. Crawford et al., Phys. Rev. C, **82**, 014311 (2010).
- [70] S. McDaniel et al., Phys. Rev. C, **81**, 024301 (2010).
- [71] D. Steppenbeck et al., Phys. Rev. C, **96**, 064310 (2017).
- [72] P. Koseoglou et al., J. Phys. Conf. Ser., **1555**(1), 012026 (2020).
- [73] R. Zidarova et al., Phys. Scr., **99**(7), 075309 (2024).
- [74] R. Zidarova et al. (2024), in preparation.
- [75] K. Wimmer et al., RIKEN Accel. Prog. Rep., **54**, S27 (2020).
- [76] The HYPATIA array, <https://www.nishina.riken.jp/collaboration/SUNFLOWER/devices/hypatia/index.php> (2024).
- [77] J. Tanaka et al., Detectors for next-generation quasi-free scattering experiments (2024), In this volume.